Progress in Natural Science: Materials International 35 (2025) 955–962

HOSTED BY

Contents lists available at ScienceDirect

Progress in Natural Science: Materials International

journal homepage: www.elsevier.com/locate/pnsmi

Fe/N Co-doped micro-mesoporous carbon nanofibers as high-performance catalysts for zinc-bromine flow batteries

Xu Wang [a,b], Qiang Zhang [a,c,d,*], Shuangjie Chu [a,e], Tong Qin [b], Qian Liu [a], Zhengzheng Li [b], Jun Wang [a], Jiayu Wan [c], Bo Mao [a,**]

[a] School of Materials Science and Engineering, Shanghai Jiao Tong University, Shanghai, 200240, China
[b] Baowu Carbon Technology Co. Ltd., Shanghai, 201999, China
[c] Future Battery Research Center, Global Institute of Future Technology, Shanghai Jiao Tong University, Shanghai, 200240, China
[d] School of Energy and Power Engineering, North University of China, Taiyuan, 030051, China
[e] Baoshan Iron & Steel Cooperation Limited, Shanghai, 201900, China

ARTICLE INFO

Keywords:
Zinc-bromine flow battery
Carbon nanofiber
Zeolitic imidazolate framework
Catalyst
Electrostatic spinning

ABSTRACT

Zinc-bromine flow batteries (ZBFBs) are promising for sustainable energy storage due to their high energy density and cost-effectiveness. However, the sluggish kinetics of the Br^2/Br^- redox reaction at the cathode limits their performance. Here, we developed Fe/N co-doped micro-mesoporous carbon nanofibers (Fe-N-CNFs) as a high-performance cathode catalyst. Synthesized via electrospinning Fe/Zn-ZIFs with PAN/PVP, followed by carbonization, the Fe-N-CNFs exhibited a hierarchical pore structure with a specific surface area of 1057 $m^2\ g^{-1}$ and an average pore size of 2.5 nm. The optimized catalyst, doped with 4 wt% Fe, achieved an energy efficiency of 81 % at 80 mA cm^{-2} and maintained a Coulombic efficiency of 98.4 % over 200 cycles. This work demonstrates the potential of integrating electrospinning with MOF-derived catalysts to enhance ZBFB performance, offering a scalable solution for high-efficiency energy storage systems.

1. Introduction

The transition from fossil fuels to renewable energy sources has become a cornerstone of efforts to mitigate climate change and address the global energy crisis [1]. Renewable energy sources, including solar and wind, are inherently intermittent and require efficient energy storage systems to enable reliable and continuous power supply [2–4]. Among the diverse energy storage technologies, zinc-bromine flow batteries (ZBFBs) stand out due to their high theoretical energy density, long cycle life, cost-effectiveness, and scalability [5]. Despite these advantages, the sluggish kinetics of the Br^2/Br^- redox reaction at the cathode severely limits their operational efficiency, particularly at high current densities, posing a significant barrier to their widespread application [6,7].

Developing advanced cathode materials has been a primary focus to overcome these challenges. Carbon-based materials such as carbon felts (CFs) and graphite felts (GFs) are commonly used as cathodes due to their excellent electronic conductivity, chemical stability, and porous structures [8–11]. However, their intrinsic catalytic activity is insufficient to support the high reaction rates required in ZBFBs. To enhance their catalytic performance, strategies involving heteroatom doping (e.g., nitrogen, sulfur) and the integration of transition metals (e.g., Fe, Co, Ni) have been extensively studied [12,13]. These modifications introduce abundant active sites and modulate the electronic structure, thereby improving the electrochemical kinetics of the redox reactions [14–16]. Transition metal-nitrogen-carbon (M-N-C) catalysts, particularly those derived from metal-organic frameworks (MOFs), have demonstrated remarkable electrocatalytic activity in various energy applications, positioning them as promising candidates for ZBFB cathodes [17–19].

Previous studies have shown that doping carbon materials with nitrogen or incorporating transition metals can significantly enhance catalytic performance [20–22]. For instance, nitrogen-doped carbon catalysts have been widely recognized for their ability to improve electron transfer and catalytic stability [23–25]. Zhang et al. reported a zeolite-derived carbon material doped with nitrogen, achieving energy efficiencies exceeding 82 % in ZBFBs at 80 mA cm^{-2} [26]. Similarly, metal-based catalysts such as Fe or Co integrated into nitrogen-doped

* Corresponding author. School of Materials Science and Engineering, Shanghai Jiao Tong University, Shanghai, 200240, China.
** Corresponding author.
E-mail addresses: zhangqiang17@sjtu.edu.cn (Q. Zhang), bmao@sjtu.edu.cn (B. Mao).

https://doi.org/10.1016/j.pnsc.2025.07.008
Received 19 June 2025; Received in revised form 27 July 2025; Accepted 29 July 2025
Available online 16 August 2025

carbon have exhibited high activity due to the formation of M − N active sites. For example, Xiang et al. demonstrated the use of nitrogen-doped carbon materials for ZBFBs, achieving a voltage efficiency of 83 % and improved mass transport properties [27]. Despite these advancements, there remains a need for scalable and structurally optimized catalysts that can meet the high-performance demands of industrial applications.

An additional challenge lies in optimizing the structural design of catalytic materials to maximize the exposure of active sites and facilitate mass transport [28]. Conventional bulk carbon materials often suffer from limited accessibility to active sites and suboptimal ion diffusion properties [29]. Addressing these issues requires the development of hierarchical structures that can combine efficient electron conductivity with enhanced mass transport. Such designs ensure improved reactant accessibility and faster kinetics, which are essential for efficient energy storage systems. Electrospinning, a scalable and versatile fabrication technique, has emerged as a powerful approach for constructing such structures [30,31]. By enabling the synthesis of carbon nanofibers (CNFs) with controlled morphology and hierarchical porosity, electrospinning provides a platform for integrating advanced catalysts with superior performance characteristics [32].

Electrospun CNFs exhibit high specific surface areas, excellent conductivity, and mechanical robustness, making them ideal platforms for integrating MOF-derived catalysts [33]. By combining electrospinning with MOF precursors, it is possible to achieve a synergistic effect, where the transition metals and nitrogen doping enhance catalytic activity, and the hierarchical pore structure facilitates efficient mass transport and reactant accessibility. For example, Jung et al. prepared mesoporous tungsten oxynitride nanofibers through electrospinning and heat treatment, achieving energy efficiencies up to 89 % in ZBFBs [34]. This highlights the potential of electrospinning techniques in fabricating high-performance electrode materials.

In this study, we report the development of Fe/N co-doped micro-mesoporous carbon nanofibers (Fe-N-CNFs) as a high-performance cathode catalyst for ZBFBs. The Fe-N-CNFs, synthesized via electrospinning a composite of Fe/Zn-ZIFs and PAN/PVP polymers, exhibited a three-dimensional hierarchical pore structure with a specific surface area of 1057 $m^2\ g^{-1}$ and an average pore size of 2.5 nm. These structural features significantly enhance reactant infiltration and active site accessibility, resulting in improved catalytic performance. The optimized catalyst, doped with 4 wt% Fe, demonstrated the highest catalytic activity, reflected in a 34 % reduction in charge transfer resistance, superior mass transport properties, and an energy efficiency of 81 % at a current density of 80 mA cm^{-2}. Furthermore, the full-cell battery maintained 98.4 % Coulombic efficiency and exhibited stable cycling performance over 200 cycles, highlighting the robustness and scalability of this design. The Fe-N-CNFs, with their hierarchical pore structure and optimized iron doping, significantly enhance catalytic activity and mass transport, resulting in improved energy efficiency and stable performance in ZBFBs.

2. Experimental section

2.1. Materials

Zinc nitrate hexahydrate (99 %), 2-methylimidazole (2-mIm, 98 %), anhydrous ferric chloride (AR), and polyvinylpyrrolidone (PVP, MW130000) were purchased from Aladdin Biochemical Technology Co., Ltd. (Shanghai, China). Methanol (≥99.5 %), ethanol (≥99.7 %), and N, N-dimethylformamide (DMF, ≥99 %) were obtained from Sinopharm Chemical Reagent Co., Ltd. (Shanghai, China). Polyacrylonitrile (PAN, MW150000) was sourced from Macklin Biochemical Technology Co., Ltd. (Shanghai, China).

2.2. Sample synthesis

Synthesis of Fe/Zn-ZIFs: Fe/Zn-ZIFs with Fe-to-Zn molar ratios of 0 %, 2 %, 4 %, and 6 % were synthesized. In a standard procedure, 11.156 g of $Zn(NO_3)_2{\cdot}6H_2O$ and 0.122 g of $FeCl_3$ were dissolved in 120 mL of methanol, and the mixture was stirred for 15 min (denoted as solution A). Next, 24.6 g of 2-methylimidazole (2-mIm) was dissolved in 120 mL of methanol and stirred for 15 min to prepare solution B. The two solutions were then rapidly combined and left to age for 24 h at room temperature. After aging, the precipitate was centrifuged, washed several times with methanol, and dried overnight at 60 °C. The resulting light reddish-brown nanocrystals (2 % Fe/Zn-ZIFs) were ground into a fine powder and used as the precursor for electrospinning.

Synthesis of Fe/Zn-ZIFs/PAN/PVP NFs: 0.4375 g of PAN and 0.0626 g of PVP were dissolved in 5 mL of DMF and stirred for 4 h while heating at 60 °C. Subsequently, 0.25 g of Fe/Zn-ZIFs nanocrystals was added and stirred continuously until a uniform dispersion was achieved. The prepared solution was transferred into a 5 mL syringe equipped with a steel needle for electrospinning. The electrospinning process was conducted by applying direct current voltages of 15 kV and −2.5 kV to the needle tip and receiver, respectively. The flow rate was maintained at 1 mL h^{-1}, and the distance between the needle and receiver was set to 12 cm. The temperature inside the electrospinning machine was 30 °C, with humidity at 30 %. The drum rotated at a speed of 150 rpm, and the spinning process lasted approximately 5 h. After spinning, the material and the collection paper were dried in a vacuum oven at 80 °C for 12 h, resulting in the formation of Fe/Zn-ZIFs nanofibers, which were subsequently used as precursors for the Fe-N-CNFs catalyst.

Synthesis of Fe-N-CNFs: The as-prepared Fe/Zn-ZIFs/PAN/PVP NFs were pre-oxidized in an air atmosphere at 270 °C for a duration of 2 h, with a heating rate of 1 °C min^{-1}. Following pre-oxidation, the nanofibers were carbonized in a nitrogen atmosphere at 800 °C for 2 h, with a heating rate of 2 °C min^{-1}, to obtain the Fe-N-CNFs catalyst.

2.3. Characterization

The crystal structure and chemical composition of the samples were characterized using X-ray diffraction (XRD, Rigaku Ultima IV, Japan) with Cu Kα radiation, scanning the 2θ range from 10° to 65°. The chemical states and surface functional groups were analyzed using X-ray photoelectron spectroscopy (XPS, Thermo ESCALAB 250Xi, USA) with monochromatic Al Kα radiation as the excitation source. The surface morphology and microstructure of the samples were examined using a scanning electron microscope (SEM, Thermo Fisher Scientific Apreo 2S, USA) and a transmission electron microscope (TEM, JEOL 2010, Japan). The specific surface areas, pore volumes, and pore size distributions were measured through nitrogen adsorption-desorption experiments using the Autosorb-IQ-MP pore size analyzer (BET, Quanta Instruments, USA) at 77 K. The mesopores were calculated using the Barrett-Joyner-Halenda (BJH) method for P/P_0 from 0.15 to 1, while the micropores were determined using the Horvath–Kawazoe equation for P/P_0 from 0 to 0.15.

2.4. Electrochemical measurements

Electrochemical measurements were conducted using an electrochemical workstation (CHI602E, Chenhua, Shanghai) in a three-electrode system at room temperature. The reference electrode used was a saturated calomel electrode (SCE) with a salt bridge, while the counter electrode was a graphite rod. For the cyclic voltammetry (CV) test, the potential scan range was 0–1.2V vs. SCE and the electrolyte consisted of 0.1 M $ZnBr_2$ and 0.1 M Br_2. The linear sweep voltammetry (LSV) test had a sweep speed of 1 mV s^{-1} in the weakly polarized region (overpotential $\eta < 25/n$) and the same electrolyte as the CV test. Electrochemical impedance spectroscopy (EIS) was performed at the open circuit voltage (OCV) by sweeping the frequencies from 0.01 HZ to 105 HZ with a waveform amplitude of 5 mV, using a 2 M $ZnBr_2$ electrolyte.

The working electrode was prepared as follows: The Fe-N-CNFs catalyst (2.5 mg) was dispersed in a mixture of 300 μL of deionized

water and 180 μL of isopropyl alcohol. The mixture was ultrasonically stirred for 30 min to achieve a uniform suspension. Subsequently, 20 μL of a 5 wt% Nafion solution was added, and the suspension was further subjected to vigorous ultrasonication for 20 min. Finally, 10 μL of the catalyst ink was drop-cast onto a glassy carbon (GC, d = 5 mm) electrode surface and naturally dried.

Full battery tests were conducted using a custom-made flow cell. The flow cell consists of end plates, fluid collectors, gaskets, electrode frames, positive and negative electrodes, a separator, and a catalyst coating membrane (CCM). The electrodes used were graphite felt (60 mm × 60 mm × 5 mm). The catalyst layer was prepared by mixing 0.045 g of Fe-N-CNFs catalyst, 10 mL of ethanol, and 0.1 g of a 5 wt% Nafion solution to form a uniform slurry. The slurry was sprayed onto the surface of a porous polypropylene membrane, which was then dried in a vacuum at 80 °C. The electrolytes used were solutions containing 2 M $ZnBr_2$, 3 M KCl, and 0.4 M MEPBr. Charge-discharge profiles were recorded using Xinwei CT-4008T-5V12A-S21-F test system under a constant-current mode. The batteries were charged at a constant areal capacity of 20 mAh cm^{-2} and then completely discharged to a cut-off voltage of 0.5 V.

3. Results and discussion

The synthetic procedure and preparation principles of the Fe-N-CNFs catalyst are illustrated in Fig. 1. The catalyst was prepared by electrospinning Fe/Zn-ZIFs/PAN/PVP composite nanofibers, followed by pre-oxidation and carbonization processes. The XRD patterns of Fe/Zn-ZIFs and Fe-N-CNFs with varying Fe content are presented in Fig. 2. In Fig. 2a, it can be observed that the diffraction peak positions and intensities of Fe/Zn-ZIFs nanocrystals with different Fe additions (0 % Fe corresponds to ZIF-8) are identical. This indicates that the addition of Fe does not affect the crystal structure of ZIF-8 material. The major peaks and planes of the ZIFs are observed at 2θ values of 7.38° (011), 10.08° (002), 12.78° (112), 14.72° (022), 16.50° (013), 18.08° (222), and 22.18° (114) are consistent with the typical diffraction patterns of ZIF-8, in agreement with previously reported values in the literature [35]. The characteristic diffraction peaks with high intensities and no additional peaks, suggesting a high crystallinity of the synthesized ZIFs sample. In Fig. 2b, two broad peaks are observed at 2θ values of 25.0° and 44.0°, which correspond to the (002) and (101) crystal plane diffractions of graphitic carbon. In comparison to the 0 % Fe-N-CNFs sample, three additional diffraction peaks are observed at 2θ values of 43.6°, 44.7°, and 51.0° in the other three samples doped with Fe. These peaks indicate the presence of Fe and Fe_3C nanoparticles, confirming the successful incorporation of Fe into the carbon matrix.

The microscopic morphology of Fe/Zn-ZIFs nanocrystals, Fe/Zn-ZIFs/PAN/PVP NFs, and Fe-N-CNFs catalysts was observed by SEM. As shown in Fig. 2c–a, the Fe/Zn-ZIFs nanocrystals exhibit a uniform dodecahedral structure, typical of ZIF-8 materials. The crystals are well-formed and exhibit smooth surfaces, indicating high crystallinity. No significant changes in shape or size were observed, suggesting that the incorporation of Fe does not affect the fundamental structure of the ZIFs. In Fig. 2c–b, a 3D network structure is observed, where Fe/Zn-ZIFs nanofibers are interconnected with polymer nanofibers through the electrospinning process. This results in a continuous fibrous network that provides structural stability to the material. The electrospun fibers maintain a uniform distribution of the Fe/Zn-ZIFs nanocrystals, ensuring consistent interaction with the surrounding material. This network structure is essential for promoting effective mass transport within the material. After pre-oxidation and carbonization, the nanofibers undergo structural changes that increase the number of defects and result in the formation of a porous surface. As shown in Fig. 2c–c, the collapse of the ZIFs structure during carbonization further enhances the porosity of the material. This porous structure, primarily due to the carbonization of the polymer fibers, contributes to the formation of carbon nanofibers. The decomposition and evaporation of PVP and zinc generate mesopores and micropores, respectively. The resulting increase in porosity enhances the accessibility of active sites and improves ion diffusion, which is crucial for the electrochemical performance of the Fe-N-CNFs catalyst. As shown in Fig. 2c, the Fe-N-CNFs exhibit a highly uniform fibrous structure with a smooth surface. The images reveal that the carbon nanofibers are relatively well-ordered, with some regions showing slight amorphous character, which is typical for carbon materials derived from polymer precursors. Additionally, the SEM analysis shows that Fe nanoparticles are encapsulated in the carbon nanofibers. These Fe particles are observed to be in the size range of 10–30 nm and appear as dark spots within the carbon matrix, confirming the successful incorporation of iron into the nanofiber structure. The presence of Fe/N co-doping is further supported by the appearance of Fe-rich domains in the SEM images, which may contribute to catalytic activity. The overall

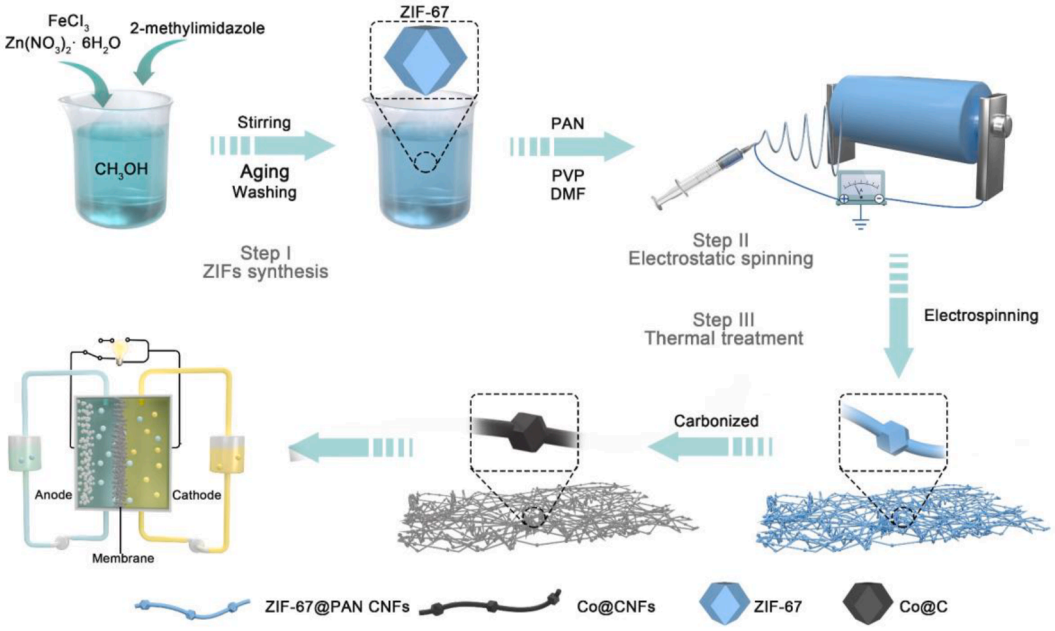

Fig. 1. Synthesis of Fe-N-CNFs catalysts.

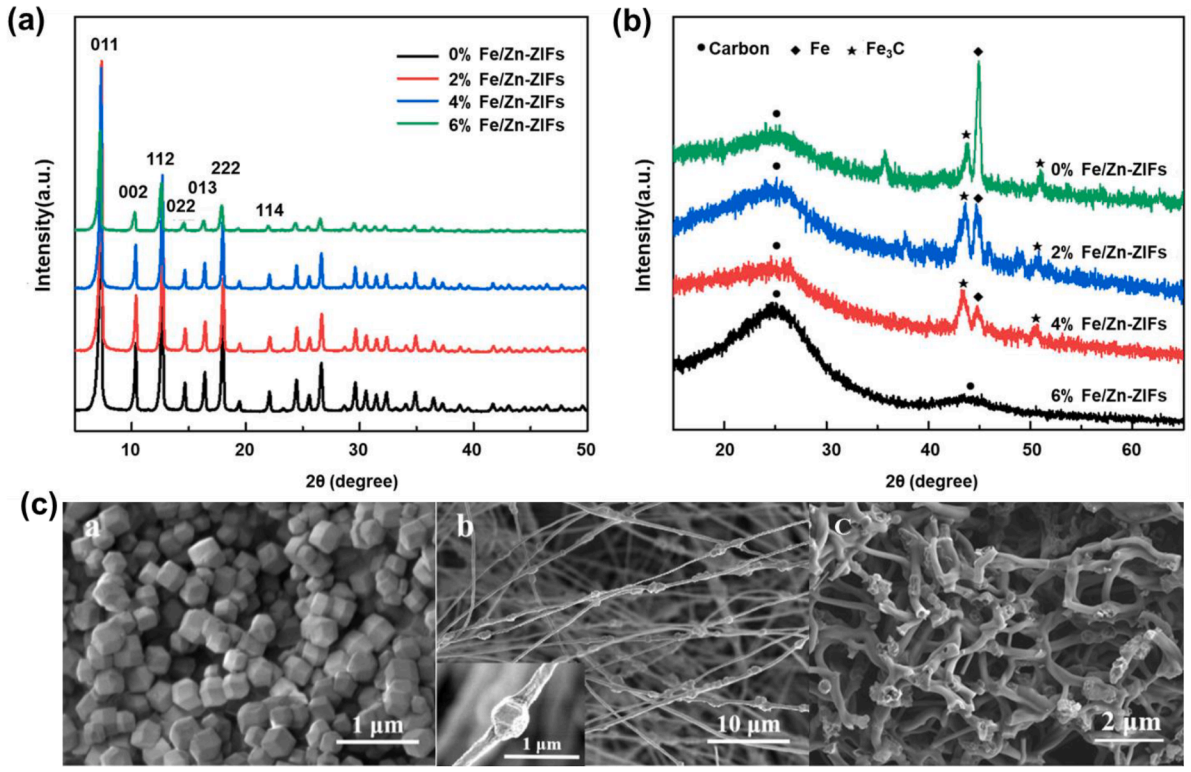

Fig. 2. XRD spectrum of (a) Fe/Zn-ZIFs and (b) Fe-N-CNFs samples, and (c) SEM images. a. Fe/Zn-ZIFs nanocrystal, b. Fe/Zn-ZIFs/PAN/PVP NFs and c. Fe-N-CNFs catalyst samples.

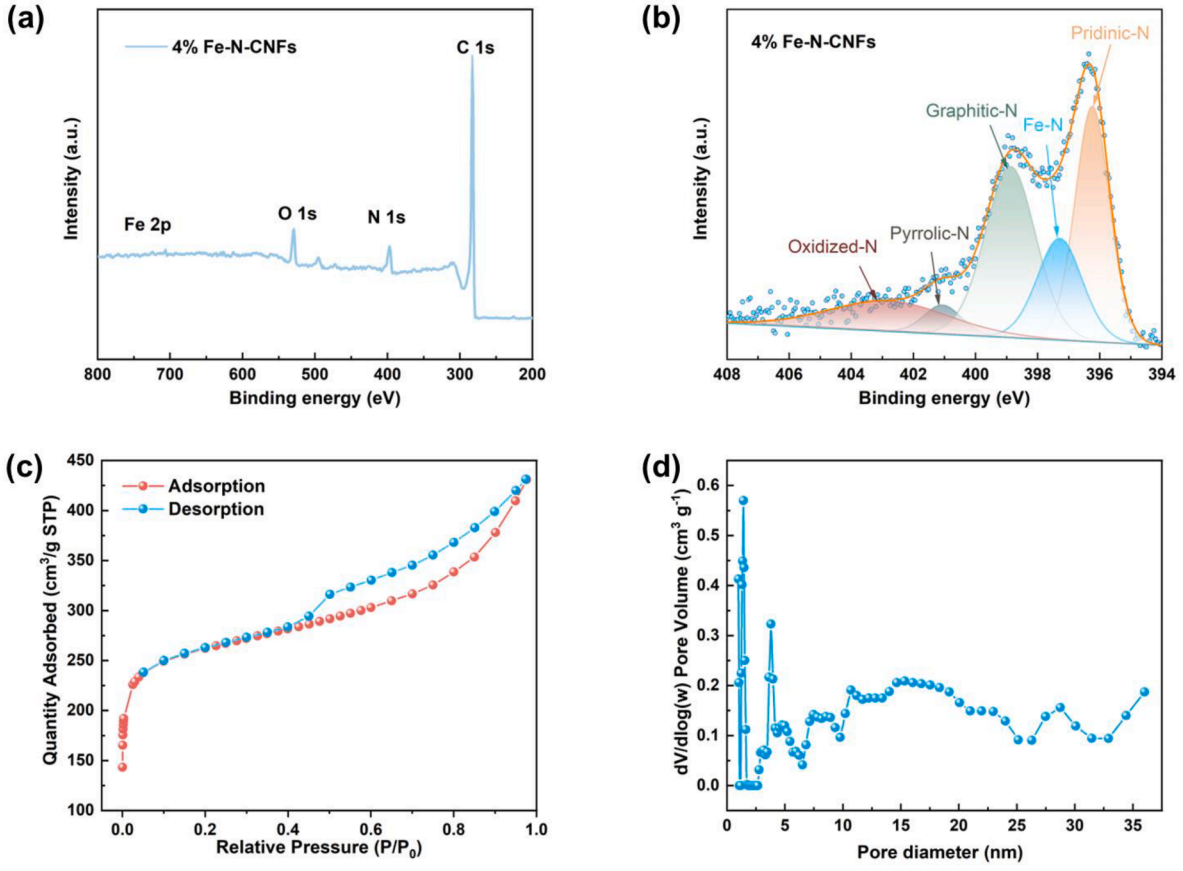

Fig. 3. (a) High-resolution XPS spectra of Fe-N-CNFs; (b) Curve fitting for the N 1s peak of Fe-N-CNFs. (c) Nitrogen adsorption-desorption isotherm of Fe-N-CNFs; (d) Pore size distribution of Fe-N-CNFs.

morphology of the Fe-N-CNFs reveals that the material retains its fibrous structure after carbonization, with the Fe nanoparticles embedded within the graphitic carbon network, facilitating efficient charge and mass transport during electrochemical reactions.

XPS analysis was performed to investigate the surface composition and chemical states of Fe-N-CNFs. The catalyst material consists of Fe, C, N, and O, and the full survey spectrum, along with the Fe 2p and N 1s spectra, are shown in Fig. 3a. The elemental composition of the 4 % Fe-N-CNFs catalyst is as follows: Fe content is 0.72 %, C content is 83.17 %, N content is 8.43 %, and O content is 7.68 %. These results confirm the successful doping of Fe atoms into the carbon matrix. The N 1s spectrum, shown in Fig. 3b, exhibits peaks at binding energies of 396.3, 397.3, 398.9, 401.1, and 402.9 eV. These peaks correspond to pyridinic nitrogen (31.13 %), Fe-N (17.56 %), graphitic nitrogen (33.07 %), pyrrole nitrogen (4.18 %), and nitrogen oxides (14.05 %), respectively. Previous studies have shown that pyridinic nitrogen and graphitic nitrogen contribute significantly to the redox catalytic activity, while Fe-N bonds are considered key active sites for catalytic reactions. The high density of active sites, especially Fe-N, is further facilitated by the porous structure of the Fe-N-CNFs, as observed in the SEM images. These sites are crucial for improving electron and ion transport during electrochemical reactions, thus boosting the catalytic efficiency.

The specific surface area and pore size distribution of the Fe-N-CNFs samples were analyzed using nitrogen adsorption-desorption experiments. The results, shown in Fig. 3c, reveal that the Fe-N-CNFs have a specific surface area of 1057.156 m^2 g^{-1} and an average pore size of

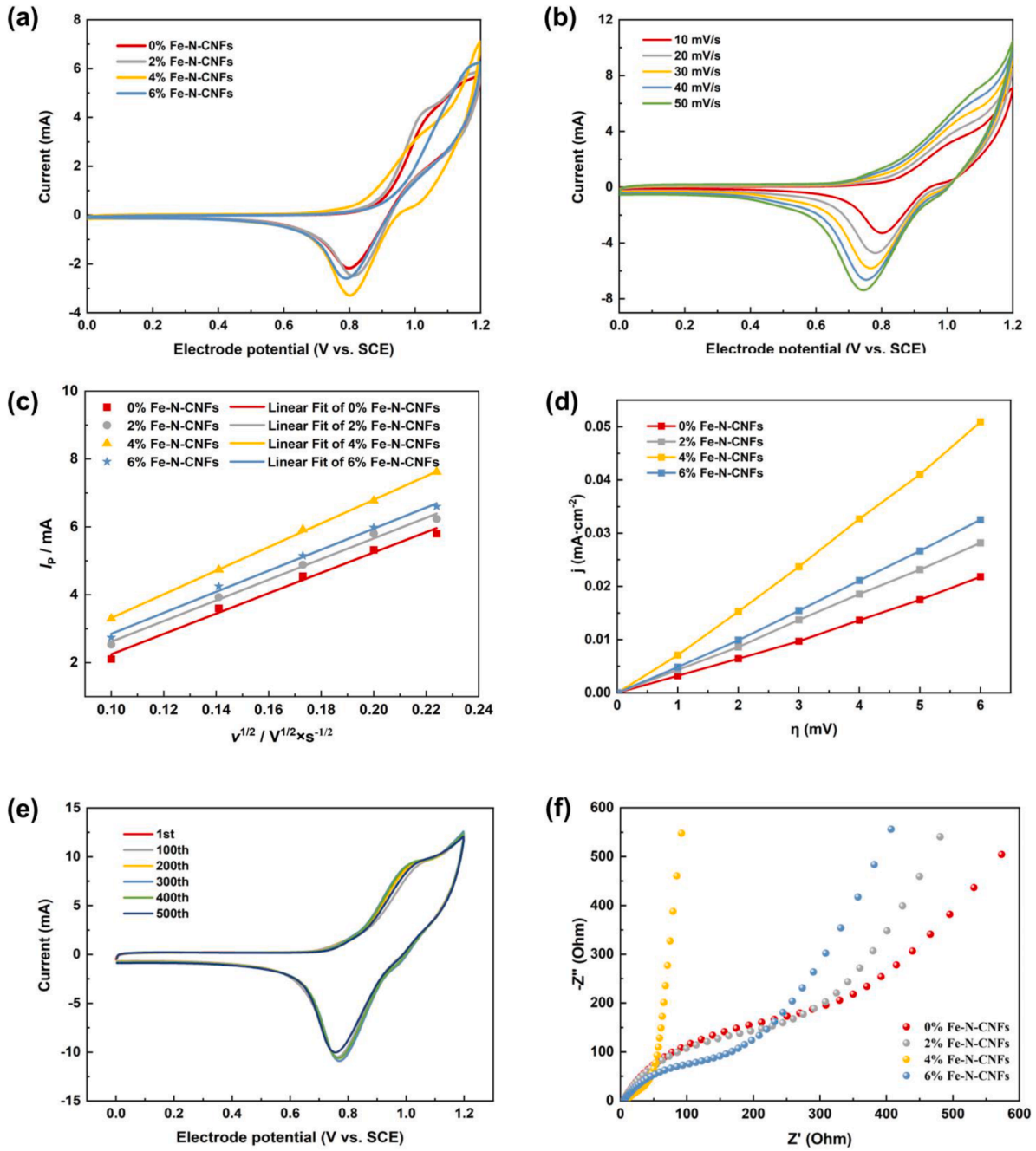

Fig. 4. (a) CV curves of samples at the scan rate of 10 mV s^{-1}; (b) CV curves of 4 % Fe-N-CNFs at different scan rates; (c) Relationship between the I_p and $v^{1/2}$ of samples; (d) LSV curve of samples at the scan rate of 1 mV s^{-1}; (e) Electrochemical activity stability tests of 4 % Fe-N-CNFs at the scan rate of 50 mV s^{-1}; (f) Nyquist plots of samples.

2.50 nm, indicating the presence of a rich and well-developed pore structure. The nitrogen adsorption-desorption isotherm of Fe-N-CNFs follows a typical IV-type isotherm curve, characterized by a distinct hysteresis loop, which is indicative of mesoporous materials. Falling within the mesoporous range, facilitates the Br_2/Br^- redox reaction by optimally matching the molecular dimensions of Br_2 (van der Waals diameter ~0.33 nm) and Br^- (ionic radius ~0.196 nm) to ensure unimpeded diffusion, balancing the high specific surface area provided by micropores with efficient mass transport through mesoporous channels. As further illustrated in Fig. 3d, the Fe-N-CNFs exhibit a multi-level pore structure consisting of both mesopores and micropores, which are attributed to the decomposition and evaporation of PVP and Zn during the carbonization process. The combination of these different pore sizes significantly increases the available surface area for reactant penetration. This multi-level pore structure not only improves the accessibility of active sites but also enhances the contact between the electrolyte and the catalyst, which in turn accelerates the Br_2/Br^- redox reaction at the electrode surface. The high specific surface area and porous nature of the Fe-N-CNFs contribute to their electrochemical performance by facilitating efficient ion diffusion and enhancing reaction kinetics.

Cyclic voltammetry tests were performed on Fe-N-CNFs samples to investigate their electrochemical activity, as shown in Fig. 4a. The results reveal that the current density follows the order of 4 % > 6 % > 2 % > 0 %, which correlates with the electrochemical reaction rates of each material. The N-CNFs catalyst without Fe exhibited the lowest current density, indicating the poorest catalytic performance and fewer effective active sites. Upon doping with Fe, the electrochemical activity of the catalyst increased, with the maximum activity observed at 4 % Fe content. However, further increasing the Fe content to 6 % led to a notable decrease in current density, suggesting the formation of metal clusters and a reduction in the exposure of effective active sites. This indicates that the optimal electrochemical catalytic activity for the Fe-N-CNFs catalyst occurs at an Fe content of 4 %. To further assess the catalyst's ability to transport active species, CV tests were conducted on the 4 % Fe-N-CNFs catalyst at various scan rates, as shown in Fig. 4b. The results show that with increasing scan rates, the double-layer response current also increased, while the reduction peak potential shifted negatively. This behavior indicates that the Br_2/Br^- redox reaction is quasi-reversible. Moreover, a linear relationship between the reduction peak current (I_p) and the square root of the scan rate ($v^{1/2}$) was observed for all samples (Fig. 4c). By comparing the slopes, it was determined that the 4 % Fe-N-CNFs catalyst exhibited the largest diffusion coefficient and the best mass transfer capacity among the tested materials. Fig. 4d shows the linear sweep voltammetry (LSV) results, where the slope of the LSV curve for different Fe-N-CNFs samples follows the order of 4 % > 6 % > 2 % > 0 %. This indicates that the 4 % Fe-N-CNFs catalyst has the highest charge transfer rate, which is consistent with the CV results. The stability of the 4 % Fe-N-CNFs catalyst was further evaluated through a long-cycle CV test (500 cycles). As shown in Fig. 4e, after 500 cycles, the catalytic activity of the 4 % Fe-N-CNFs remained nearly

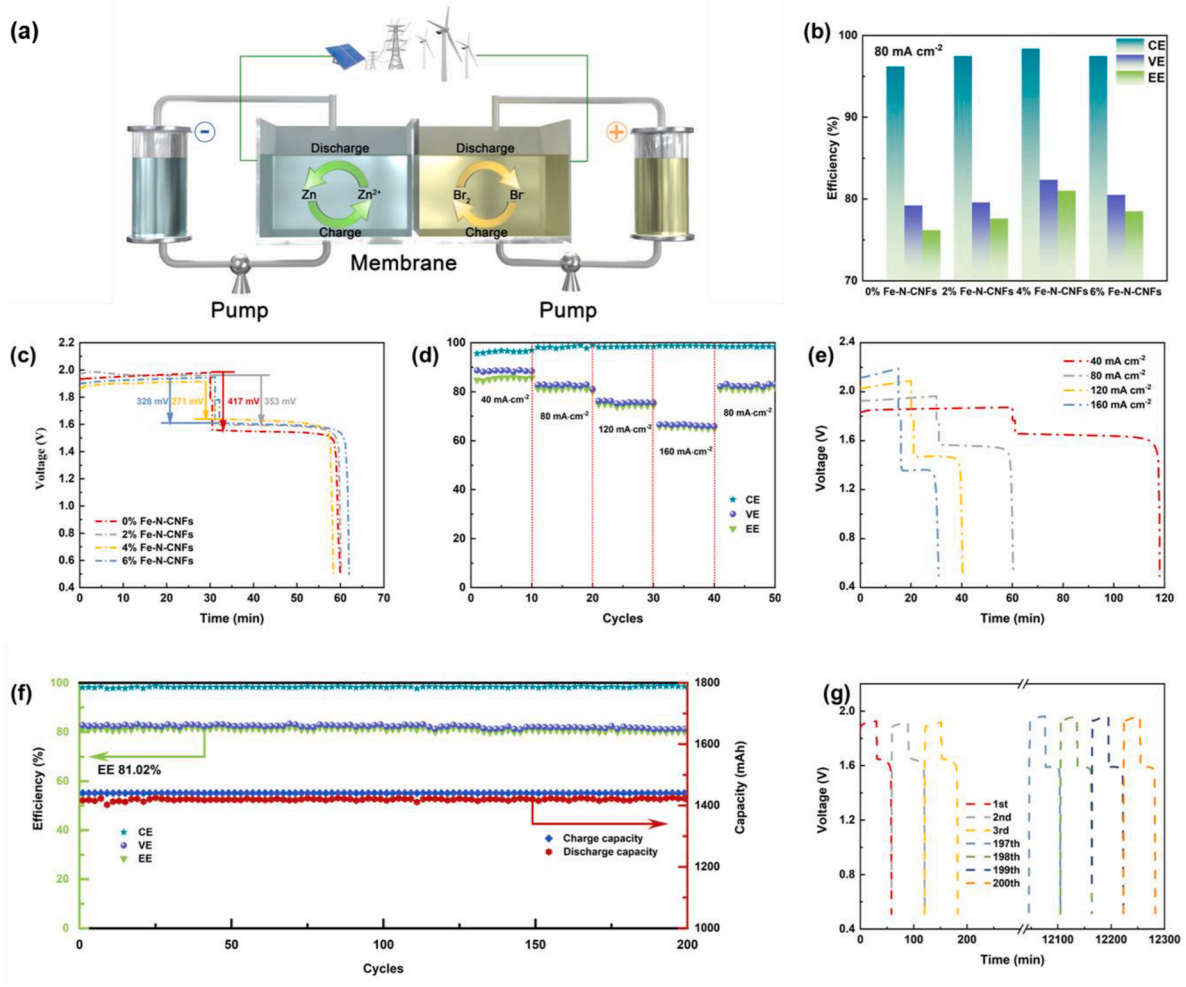

Fig. 5. (a) Application diagram of zinc bromine flow battery. (b) The efficiency of the ZBFB with Fe-N-CNFs at a current density of 80 mA cm^{-2}; (c) The charge-discharge curves for ZBFB with Fe-N-CNFs at 80 mA cm-2; (d) The efficiency of the ZBFB with 4 % Fe-N-CNFs at different current densities; (e) The charge-discharge curves for ZBFB with 4 % Fe-N-CNFs at different current densities; (f) Cycle performance of the ZBFB with 4 % Fe-N-CNFs at 80 mA cm^{-2}; (g) 1–3 and 197–200 cycles of the ZBFB with 4 % Fe-N-CNFs at 80 mA cm^{-2}.

unchanged, demonstrating excellent stability over extended cycling. Finally, the impedance of the samples was examined through electrochemical impedance spectroscopy (EIS), with the results shown in Fig. 4f. The EIS spectrum consists of a semicircle at high frequencies and a straight line at low frequencies. Notably, the 4 % Fe-N-CNFs sample exhibited the smallest ion diffusion resistance and charge transfer resistance, consistent with the results from previous CV and LSV tests.

To evaluate the feasibility and performance of the Fe-N-CNFs catalyst, full-cell zinc-bromine flow batteries were further tested (Fig. 5a). As shown in Fig. 5b, the battery efficiency of ZBFBs with different Fe content in the Fe-N-CNFs catalyst was evaluated at a current density of 80 mA cm^{-2}. The results indicate that the battery prepared with 4 % Fe-N-CNFs exhibits the highest coulombic efficiency of 98.4 %, voltage efficiency of 82.4 %, and energy efficiency of 81 %, outperform several recently reported ZBFB catalysts such as ZIF-derived N-doped carbon (68 % energy efficiency) [25]. These results highlight the superior electrochemical performance of the 4 % Fe-N-CNFs catalyst. The high efficiency suggests that the Fe-N-CNFs catalyst effectively mitigates self-discharge effects and enhances the overall performance of the battery. The catalyst's three-dimensional, multi-level porous network structure plays a critical role in increasing the number of active sites for electrochemical reactions, while also reducing polarization phenomena that can hinder performance, enabling a more efficient electron and ion transfer process. Furthermore, Fig. 5c shows the charge-discharge curve of the battery prepared with 4 % Fe-N-CNFs, which demonstrates the highest discharge plateau, the lowest charging platform, and the longest discharge time compared to the other catalysts. This indicates that the 4 % Fe-N-CNFs catalyst exhibits the best voltage efficiency, as it maintains a stable discharge voltage and reduces the loss during charging, thus improving the battery's overall energy utilization. This is also directly related to its structural characteristics of high specific surface area and multi-level porosity. In Fig. 5d and e, the efficiency and charge-discharge performance of the 4 % Fe-N-CNFs battery are shown under different current densities ranging from 40 to 160 mA cm^{-2}. As the current density increases, the charging time decreases, leading to a reduction in the penetration phenomenon, which allows for higher Coulombic efficiency. However, the increased current density also leads to a rise in polarization, resulting in a decrease in voltage efficiency. This trade-off highlights the importance of optimizing current density to balance charging time, CE, and VE, with the 4 % Fe-N-CNFs battery providing the best overall performance under moderate current densities. Additionally, the long-term stability of the 4 % Fe-N-CNFs catalyst was evaluated by performing continuous operation over 200 cycles at a current density of 80 mA cm^{-2}, as shown in Fig. 5f and g. The charge-discharge platform and battery efficiency showed minimal degradation after 200 cycles, indicating excellent cycle stability. The charge-discharge curves of the first three cycles and the last four cycles did not exhibit significant changes, further confirming the robust performance and long-term stability of the 4 % Fe-N-CNFs catalyst. The high stability can be attributed to the structural integrity of the Fe-N-CNFs catalyst, which is enhanced by the multi-level porous structure, as well as the strong Fe-N bonds. This stability is crucial for practical applications in energy storage systems, as it ensures reliable performance over extended use.

4. Conclusions

The Fe/Zn-ZIFs/PAN/PVP composite nanofibers were prepared via electrospinning, followed by pre-oxidation and carbonization to obtain a networked Fe-N-CNFs catalyst. The successful doping of Fe and N elements, along with uniform coating on the nanofiber surface, was achieved. The resulting three-dimensional, multi-level pore structure enhances mass transfer of reactants, improves contact with active sites, and accelerates the Br^2/Br^- redox reaction, thereby reducing electrochemical polarization. Electrochemical results demonstrate that the 4 % Fe-doped Fe-N-CNFs catalyst exhibits the highest electrochemical activity, characterized by superior mass transfer capability, minimal ion diffusion resistance, and low charge transfer resistance. Full battery tests show that, at a current density of 80 mA cm^{-2}, the zinc-bromine flow battery assembled with 4 % Fe-N-CNFs achieves a voltage efficiency of 82.4 % and an energy efficiency of 81.0 %. Furthermore, this performance remains stable over 200 cycles, demonstrating the potential of Fe-N-CNFs as an effective positive electrode material for zinc-bromine flow batteries. This work thus presents a novel strategy for designing high-performance positive electrodes, contributing to the advancement of zinc-bromine flow battery energy storage systems.

CRediT authorship contribution statement

Xu Wang: Writing – original draft, Methodology, Investigation, Formal analysis, Conceptualization. **Qiang Zhang:** Writing – review & editing, Methodology, Conceptualization. **Shuangjie Chu:** Methodology, Conceptualization. **Tong Qin:** Formal analysis. **Qian Liu:** Formal analysis. **Zhengzheng Li:** Formal analysis. **Jun Wang:** Formal analysis. **Jiayu Wan:** Writing – review & editing, Formal analysis, Conceptualization. **Bo Mao:** Writing – review & editing, Formal analysis, Conceptualization.

Data availability statement

The authors confirm that the data supporting the findings of this study are available within the article.

Declaration of competing interest

The authors declare that they have no known competing financial interests or personal relationships that could have appeared to influence the work reported in this paper.

Acknowledgments

Bo Mao acknowledgments the funding support from Excellent Youth Overseas Project of National Science and Natural Foundation of China (23Z9902016440).

References

[1] A. Olabi, M.A. Abdelkareem, Renewable energy and climate change, Renew. Sustain. Energy Rev. 158 (2022) 112111.
[2] W. Wang, B. Yuan, Q. Sun, R. Wennersten, Application of energy storage in integrated energy systems-A solution to fluctuation and uncertainty of renewable energy, J. Energy Storage 52 (2022) 104812.
[3] F. Wang, X. Wu, X. Yuan, Z. Liu, Y. Zhang, L. Fu, Y. Zhu, Q. Zhou, Y. Wu, W. Huang, Latest advances in supercapacitors: from new electrode materials to novel device designs, Chem. Soc. Rev. 46 (22) (2017) 6816–6854.
[4] H. Kojima, K. Nagasawa, N. Todoroki, Y. Ito, T. Matsui, R. Nakajima, Influence of renewable energy power fluctuations on water electrolysis for green hydrogen production, Int. J. Hydrogen Energy 48 (12) (2023) 4572–4593.
[5] R. Shan, J. Reagan, S. Castellanos, S. Kurtz, N. Kittner, Evaluating emerging long-duration energy storage technologies, Renew. Sustain. Energy Rev. 159 (2022) 112240.
[6] S. Choudhury, Review of energy storage system technologies integration to microgrid: types, control strategies, issues, and future prospects, J. Energy Storage 48 (2022) 103966.
[7] X. Lin, R. Zamora, Controls of hybrid energy storage systems in microgrids: critical review, case study and future trends, J. Energy Storage 47 (2022) 103884.
[8] W. Liu, Z. Zhao, T. Li, S. Li, H. Zhang, X. Li, A high potential biphenol derivative cathode: toward a highly stable air-insensitive aqueous organic flow battery, Sci. Bull. 66 (5) (2021) 457–463.
[9] W. Lu, P. Xu, S. Shao, T. Li, H. Zhang, X. Li, Multifunctional carbon felt electrode with N-rich defects enables a long-cycle zinc-bromine flow battery with ultrahigh power density, Adv. Funct. Mater. 31 (30) (2021) 2102913.
[10] S. Suresh, M. Ulaganathan, R. Pitchai, Realizing highly efficient energy retention of Zn-Br_2 redox flow battery using rGO supported 3D carbon network as a superior electrode, J. Power Sources 438 (2019) 226998.
[11] R. pandiyan Naresh, A. Surendran, P. Ragupathy, D. Dixon, Enhanced electrochemical performance of zinc/bromine redox flow battery with carbon-nanostructured felt generated by cobalt ions, J. Energy Storage 52 (2022) 104913.
[12] C. Wang, W. Lu, Q. Lai, P. Xu, H. Zhang, X. Li, A TiN nanorod array 3D hierarchical composite electrode for ultrahigh-power-density bromine-based flow batteries, Adv. Mater. 31 (46) (2019) e1904690.

[13] Z. Xu, Q. Fan, Y. Li, J. Wang, P.D. Lund, Review of zinc dendrite formation in zinc bromine redox flow battery, Renew. Sustain. Energy Rev. 127 (2020) 109838.
[14] L. Tang, T. Li, W. Lu, X. Li, Lamella-like electrode with high Br_2-entrapping capability and activity enabled by adsorption and spatial confinement effects for bromine-based flow battery, Sci. Bull. 67 (13) (2022) 1362–1371.
[15] R. Wang, Y. Li, H. Liu, Y.-L. He, M. Hao, Sandwich-like multi-scale hierarchical porous carbon with a highly hydroxylated surface for flow batteries, J. Mater. Chem. A 9 (4) (2021) 2345–2356.
[16] W. Xia, K. Xie, S. Gao, Z. Song, L. Chen, C. Li, Multidentate chelating ligands enable high-performance zinc-bromine flow batteries, Angew. Chem. Int. Ed. 137 (6) (2025) e202418669.
[17] L. Tang, W. Lu, H. Zhang, X. Li, Progress and perspective of the cathode materials towards bromine-based flow batteries, Energy Mater. Adv. 2022 (2022) 9850712.
[18] K.S. Archana, R.p. Naresh, H. Enale, V. Rajendran, A.M.V. Mohan, A. Bhaskar, P. Ragupathy, D. Dixon, Effect of positive electrode modification on the performance of zinc-bromine redox flow batteries, J. Energy Storage 29 (2020) 101462.
[19] C. Jin, H. Lei, M. Liu, A. Tan, J. Piao, Z. Fu, Z. Liang, H. Wang, Low-dimensional nitrogen-doped carbon for Br2/Br− redox reaction in zinc-bromine flow battery, Chem. Eng. J. 380 (2020) 122606.
[20] K. Mariyappan, R. Velmurugan, B. Subramanian, P. Ragupathy, M. Ulaganathan, Low loading of Pt@ Graphite felt for enhancing multifunctional activity towards achieving high energy efficiency of Zn-Br_2 redox flow battery, J. Power Sources 482 (2021) 228912.
[21] Y. Yin, S. Wang, Q. Zhang, Y. Song, N. Chang, Y. Pan, H. Zhang, X. Li, Dendrite-free zinc deposition induced by tin-modified multifunctional 3D host for stable zinc-based flow battery, Adv. Mater. 32 (6) (2020) 1906803.
[22] Y. Cho, J.G. Kim, D.H. Kim, C. Pak, Achieving unprecedented cyclability of flowless zinc-bromine battery by nitrogen-doped mesoporous carbon on thick graphite felt electrode, Chem. Eng. J. 490 (2024) 151538.
[23] R. Wang, Y. Li, Y. Wang, Z. Fang, Phosphorus-doped graphite felt allowing stabilized electrochemical interface and hierarchical pore structure for redox flow battery, Appl. Energy 261 (2020) 114369.
[24] M. Wu, T. Zhao, R. Zhang, L. Wei, H. Jiang, Carbonized tubular polypyrrole with a high activity for the Br_2/Br^- redox reaction in zinc-bromine flow batteries, Electrochim. Acta 284 (2018) 569–576.
[25] J. Li, Z. Xu, M. Wu, Reaction kinetics and mass transfer synergistically enhanced electrodes for high-performance zinc–bromine flow batteries, ACS Appl. Mater. Interfaces 17 (17) (2024) 25206–25215.
[26] R. Naresh, K. Satchidhanandam, K.R. Ilancheran, B. Ambrose, M. Kathiresan, P. Ragupathy, Bimetallic metal-organic framework: an efficient electrocatalyst for bromine-based flow batteries, J. Mater. Chem. A 12 (24) (2024) 14669–14678.
[27] Q. Zhang, H. Jiang, S. Liu, Q. Wang, J. Wang, Z. Zhou, Q. Wang, Redox-targeting catalyst developing new reaction path for high-power zinc-bromine flow batteries, J. Power Sources 601 (2024) 234286.
[28] C. Wang, H. Yang, Y. Zhang, Q. Wang, NiFe alloy nanoparticles with hcp crystal structure stimulate superior oxygen evolution reaction electrocatalytic activity, Angew. Chem. Int. Ed. 58 (18) (2019) 6099–6103.
[29] S. Anantharaj, S. Kundu, S. Noda, "The Fe Effect": a review unveiling the critical roles of Fe in enhancing OER activity of Ni and Co based catalysts, Nano Energy 80 (2021) 105514.
[30] J.T. Liu, Y. Xie, Q. Gao, F.H. Cao, L. Qin, Z.Y. Wu, W. Zhang, H. Li, C.L. Zhang, 1D MOF-derived N-doped porous carbon nanofibers encapsulated with Fe_3C nanoparticles for efficient bifunctional electrocatalysis, Eur. J. Inorg. Chem. 2020 (6) (2020) 581–589.
[31] L. Gao, X. Gao, P. Jiang, C. Zhang, H. Guo, Y. Cheng, Atomically dispersed iron with densely exposed active sites as bifunctional oxygen catalysts for zinc-air flow batteries, Small 18 (8) (2022) 2105892.
[32] F. Wang, T. Feng, X. Jin, Y. Zhou, Y. Xu, Y. Gao, H. Li, J. Lei, Atomic Co/Ni active sites assisted MOF-derived rich nitrogen-doped carbon hollow nanocages for enhanced lithium storage, Chem. Eng. J. 420 (2021) 127583.
[33] Y. Wang, X. Cui, L. Peng, L. Li, J. Qiao, H. Huang, J. Shi, Metal-nitrogen-carbon catalysts of specifically coordinated configurations toward typical electrochemical redox reactions, Adv. Mater. 33 (34) (2021) 2100997.
[34] H. Jung, J. Lee, J. Park, K. Shin, H.T. Kim, E. Cho, A mesoporous tungsten oxynitride nanofibers/graphite felt composite electrode with high catalytic activity for the cathode in Zn-Br flow battery, Small (2023) 2208280.
[35] D.D. Kachhadiya, Z.V.P. Murthy, Preparation and characterization of ZIF-8 and ZIF-67 engineered PVDF mixed-matrix membranes: stability enhancement in pervaporation study, Environ. Sci. Water Res. Technol. 9 (5) (2023) 1502–1517.